arXiv:1404.5827v2 [q-bio.SC] 12 May 2014

Studying Protein Assembly with Reversible Brownian Dynamics of Patchy Particles

Heinrich C. R. Klein

Institute for Theoretical Physics, Heidelberg University, 69120 Heidelberg, Germany

Ulrich S. Schwarz*

Institute for Theoretical Physics, Heidelberg University, 69120 Heidelberg, Germany and

BioQuant, Heidelberg University, 69120 Heidelberg, Germany

(Dated: May 13, 2014)

Assembly of protein complexes like virus shells, the centriole, the nuclear pore complex or the actin cytoskeleton is strongly determined by their spatial structure. Moreover it is becoming increasingly clear that the reversible nature of protein assembly is also an essential element for their biological function. Here we introduce a computational approach for the Brownian dynamics of patchy particles with anisotropic assemblies and fully reversible reactions. Different particles stochastically associate and dissociate with microscopic reaction rates depending on their relative spatial positions. The translational and rotational diffusive properties of all protein complexes are evaluated on-the-fly. Because we focus on reversible assembly, we introduce a scheme which ensures detailed balance for patchy particles. We then show how the macroscopic rates follow from the microscopic ones. As an instructive example, we study the assembly of a pentameric ring structure, for which we find excellent agreement between simulation results and a macroscopic kinetic description without any adjustable parameters. This demonstrates that our approach correctly accounts for both the diffusive and reactive processes involved in protein assembly.

* ulrich.schwarz@bioquant.uni-heidelberg.de

I. INTRODUCTION

Assembly of biomolecules into supramolecular complexes is at the heart of many biological processes and the dynamic interplay of the different components leads to biological functionality. The most important type of self-assembling biomolecules are proteins. Although they often have a globular shape, protein assemblies can be strongly anisotropic due to the localized binding interactions between the proteins. Like biological systems in general, protein assemblies are operative on many different scales. Their size ranges from the nanometer-scale (for example for two-component complexes like Barnase and Barstar [1]) through tens of nanometers (for example for viruses, which typically consist of small multiples of 60 components [2, 3]) up to the micrometer scale (for example the mitotic spindle [4–6]). Even in steady state most biological complexes remain highly dynamic, with association events being balanced by dissociation events. Prominent examples are nuclear pore complexes [7–9] or focal adhesions[10–12]. Another important example for the dynamic nature of biological complexes are actin filaments [13–15], which are called *living polymers* due to their continuous exchange dynamics. [16] Similar to the broad range of length scales, association rate constants observed in biological systems span a wide spectrum ranging from $< 10^3$ $M^{-1}s^{-1}$ up to $> 10^9$ M^{-1} s^{-1}. [17] The highly dynamic nature of biological assemblies as well as the large range of involved spatial and temporal scales renders this physical problem challenging but fascinating.

Interestingly, recent advances in the fabrication of functionalized colloids with directional interactions (*patchy particles*) make it possible to design elementary building blocks of micrometer sizes which can be used to self-assemble complexes with new functionality. Experimental techniques ranging from DNA-mediated self-assembly [18–21] to entropic depletion interactions [22, 23] have been rapidly advancing during the last decade, thus providing a plethora of possibilities to fabricate colloidal particles whose shape and interactions can be controlled in detail. Moreover external stimuli such as temperature, light or pH can be used to control the inter-particle interactions during the assembly process . [24, 25] These techniques allow for a state- or time-dependent switching of the interactions and can be used to steer the assembly process. Controlling the particle interactions during the assembly process can prevent kinetic trapping resulting in a higher yield of the desired structure, as has recently been shown in a computational study for virus assembly. [26] To fully exploit

the potential of these techniques, a detailed understanding of the dynamics of the assembly process (distribution of intermediates, relevant time scales) is of crucial importance.

Understanding the mechanisms governing chemical reactions has a long tradition in theoretical physics and chemistry. The most powerful analytical technique in this context is the Fokker-Planck or Smoluchowski equation, which has been used early to study bimolecular association based on diffusive motion. This approach was pioneered by Smoluchowski who first calculated the maximum diffusion-limited reaction rate for a fully reactive spherical particle . [27] An important generalization of this result was derived by Collins and Kimball [28] who studied the effect of finite reactivity by introducing a radiation boundary condition relating the concentration at contact to the reactive flux. Another essential extension is the case of particles with anisotropic reactivity (*patchy particles*) . [29–34] However, most of these generalizations focus on the calculation of association rates and only a few aim at describing reversible reactions. [35, 36]

To study the full dynamics of protein assembly one needs to consider both association and dissociation processes. Moreover, even for globular proteins the intermediates formed during the assembly process are often of highly non-spherical geometry, thus rendering an analytical treatment of assembly in the framework of the Fokker-Planck equation very difficult. In this case computer simulations provide a valuable alternative. While detailed molecular dynamics (MD) simulations have been successfully used to investigate the behavior of a single molecule in great detail, studying the dynamics of large protein complexes on biologically relevant time and length scales is prohibited by the high computational costs of these simulations. Therefore coarse-grained models are required for this case. Brownian dynamics (BD) simulations, the numerical counterpart to the Fokker-Planck equation, have been extensively used to study bimolecular association kinetics with realistic protein shapes. [1, 37–45] These studies have been focused mainly on a detailed calculation of association rates in bimolecular reactions based on realistic protein shapes and binding interactions. To study reaction dynamics in a large system consisting of many proteins, various simulation frameworks have been developed. [46] They range from space- and time-continuous BD simulations as for example in the Smoldyn framework [47, 48] through event-driven tools like Greens functions reaction dynamics (GFRD) [49–51], which is based on the analytical solution of the Fokker-Planck equation, up to a space-discretized version of Gillespie's chemical master equation approach [52], as for example used in MesoRD [53–55]. While these simula-

tion frameworks have been successfully used to study reaction kinetics on a large scale, they cannot be used to study the details of assembly processes as all of these frameworks lack a detailed description of protein anisotropy, including their shape or directional interactions. To study the assembly of virus capsids as a paradigm of a biological self-assembly process for which these elements are essential, coarse-grained MD simulations [56–59] and Monte Carlo (MC) techniques [60–63] have been used. Similarly the interaction of colloidal particles has been investigated on various scales with different simulation techniques [21], including MD simulations [64], MC simulations [65, 66] and BD studies [67, 68].

Here we introduce a simulation framework which allows us to study the spatial and stochastic aspects of protein assembly to large detail and nevertheless is computationally relatively cheap. In our approach, we combine BD of realistic protein shapes with stochastic reactivity for both, association and dissociation. Proteins are described as assemblies of spheres equipped with reactive patches. Their motion in real and orientation space is based on the overdamped Langevin equation with an anisotropic diffusion tensor. Inspired by the notion of an encounter complex [1, 17, 28, 36, 43, 69, 70], we decompose the reaction process into a diffusion and a reaction part. Upon the diffusive formation of an encounter, two particles can stochastically react with a microscopic reaction rate and thus form a bond. Similarly an existing bond can be disrupted with a microscopic dissociation rate. We first show how these microscopic reaction rates can be related to macroscopic, experimentally measurable rates. We then verify that our algorithm correctly reproduces the macroscopically expected equilibrium behavior for bimolecular reactions. Finally we investigate the assembly of a pentameric ring structure and compare our simulation results to a macroscopic rate equation approach. Here we again find excellent agreement between the stochastic simulations and the macroscopic description if the macroscopic rates are calculated without any free parameter in the correct way that includes both the diffusive and reactive contributions. These results show the importance of including spatial and orientational effects as well as realistic diffusion properties to understand the dynamics governing protein assembly.

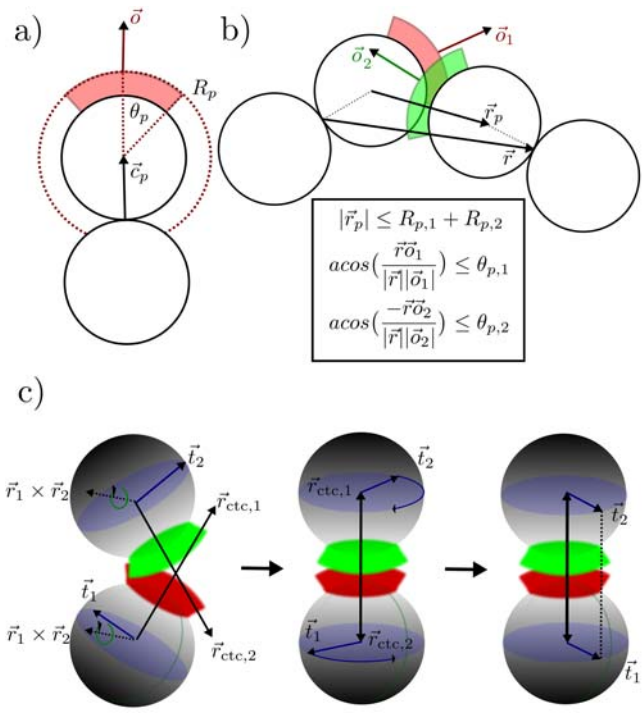

FIG. 1. Model definition. a) A dumbbell-shaped protein modeled by two hard spheres. The protein is covered with a patch of radius R_p whose center coincides with the center of one of the steric spheres and is thus shifted by $\vec{c}_p$ relative to the center of the protein (contact point of the spheres). The patch has an opening angle of θ_p around the orientation vector $\vec{o}$ pointing along the long axis of the dumbbell. b) The encounter between two of the proteins of a). Here $\vec{r}$ is the center-to-center(ctc)-vector between the proteins and $\vec{r}_p$ is the center-to-center vector between the patches. c) Illustration of the reorientation processes upon reaction. In a first step the ctc vectors of the proteins are aligned with the desired ctc-vectors. In a next step the projection of the torsion vectors $\vec{t}_1$ and $\vec{t}_2$ on a plane perpendicular to $\vec{r}_{\text{ctc}}$ are aligned. Finally the clusters are shifted so that the desired relative distance between the proteins is achieved.

II. MODEL AND METHODS

A. Encounter complex

Our simulation approach is based on the concept of the encounter complex. [1, 17, 28, 36, 43, 69, 70] In this concept a bimolecular reaction is decomposed into two steps: the undirected diffusive motion of the two binding partners A and B until they stochastically

reach the encounter state $A \cdot B$ and the reaction from the encounter state to the bound complex C. In terms of the free energy landscape the encounter complex represents a barrier separating the flat diffusive energy landscape from the reaction funnel. Thus, it is a transient state which can be characterized by the onset of highly correlated motion between the binding partners. [43] A barrier in the free energy landscape might arise for example due to a necessary rearrangement of the binding site or due to a reorganization of the water layer. In some cases there might not exist an explicit barrier, but even then the encounter complex is a helpful theoretical concept. Considering the encounter complex as the "watershed" between diffusion and reaction processes, the bimolecular reaction can be split according to the following reaction scheme:

$$A + B \underset{k_-}{\overset{k_+}{\rightleftharpoons}} C \tag{1}$$

$$A + B \underset{k_{D,b}}{\overset{k_D}{\rightleftharpoons}} A \cdot B \underset{k_d}{\overset{k_a}{\rightleftharpoons}} C. \tag{2}$$

Here k_+ and k_- represent the overall kinetic rates of the reaction. In Eq. 2 the binding and unbinding process is split into a diffusive part represented by the rates k_D and $k_{D,b}$ and a reaction part represented by k_a and k_d, respectively. Separating the binding process in free diffusive motion without steering forces and localized binding requires short-ranged interactions. Thus, our approach for the simulation of protein association corresponds to a regime of high salt concentration screening long-ranged electrostatic forces. Indeed this is a reasonable assumption for physiological salt conditions. Moreover, our approach can be used to study the assembly of μm-sized colloids functionalized with reactive patches where the size of the reactive region is small compared to the particle size. As we consider a situation in which the interaction between the proteins is short-ranged and only affects the reaction probabilities in the encounter state, individual clusters undergo free diffusive motion without an additional drift term. Moreover, here we do not consider hydrodynamic interactions which also might influence the binding kinetics.

B. Patchy particles

Our simulation system can be decomposed into four elementary structures: proteins, patches, bonds, clusters. Clusters are rigid objects that can consist of a single or of multiple proteins held together by bonds. Two clusters can react with each other by bond formation

between adhesive patches. A cluster consisting of multiple proteins can decay into smaller clusters by bond dissociation. Proteins are described by sets of non-overlapping, hard spheres approximating their shape. The proteins are equipped with reactive patches which reflect the localized binding sites. A patch is defined starting from a sphere of radius R_p whose center $\vec{c}_p$ (relative to the protein) can be chosen independent of the center of the protein. In addition, each patch is described by an orientation vector $\vec{o}$. As a simple example for a non-globular protein, in Fig. 1a we schematically show a dumbbell-shaped protein consisting of two hard spheres in contact. The protein is equipped with one reactive patch of radius R_p whose center coincides with the center of one of the steric spheres and is thus shifted by $\vec{c}_p$ from the protein center located at the contact point of the steric spheres. The orientation vector $\vec{o}$ points along the long axis of the dumbbell. Using the above definitions we formulate the following set of equations to define the encounter between two clusters mediated by a pair of patches, compare Fig. 1b:

$$r_p \leq R_{p,1} + R_{p,2} \tag{3}$$

$$\text{acos}\big(\frac{\vec{r}\cdot\vec{o}_1}{|\vec{r}||\vec{o}_1|}\big) \leq \theta_{p,1},\ \text{acos}\big(\frac{-\vec{r}\cdot\vec{o}_2}{|\vec{r}||\vec{o}_2|}\big) \leq \theta_{p,2}. \tag{4}$$

Eq. 3 means that the distance r_p between the centers of the two patches has to be sufficiently small for an encounter to occur and can be implemented easily in a simulation. Eq. 4 is more complex. It involves the center-to-center vector $\vec{r}$ and not only reflects that the patches are anisotropic, but also assumes that an encounter only occurs if the two partners have a favorable orientation relatively to each other which is defined by the two parameters $\theta_{p,1}$ and $\theta_{p,1}$. In general an anisotropic protein can be described by multiple spheres and the center of the patches can be chosen independent of the steric spheres, allowing for a variable description of proteins and their localized interactions.

C. Particle motion

In our approach particle motion is described by the six-dimensional, overdamped Langevin equation (Brownian motion) describing translational and rotational diffusion of an arbitrarily shaped but rigid object [71, 72]:

$$\partial_t \mathbf{X}_t = \mathbf{g}_t \text{ with: } \langle \mathbf{g}_t \rangle = 0,\ \langle \mathbf{g}_t \mathbf{g}_{t'} \rangle = 2k_B T \mathbf{M} \delta(t - t'). \tag{5}$$

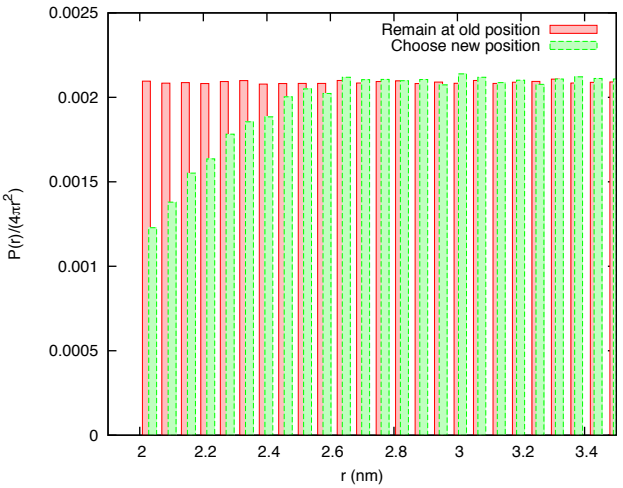

FIG. 2. Rejection methods. The distance distribution of two hard spheres of radius $R = 1$nm in a periodic box of volume $V_{\text{box}} = (8\text{nm})^3$ is shown for two different rejection methods. In the first rejection method (green) new positions of the particles are chosen (starting from their positions before collision) until no overlap is observed. In the second rejection method (red) the spheres are set back to their position before the collision. The simulations were performed at a time-step resolution of $\Delta t = 0.1$ns.

Here $\mathbf{X}_t$ is a six-dimensional position vector describing the position and orientations at time t and $\mathbf{g}_t$ is Gaussian white noise. $\mathbf{M}$ is the mobility matrix which is calculated on-the-fly for any cluster shape [71–73] following the method of de la Torre [74]. Because intermediates continuously grow and shrink due to association and dissociation, the diffusive properties of the involved clusters are continuously changing during a simulation.

Protein particles are modeled as hard spheres and their collision requires special attention. In a BD framework, particle velocities are not defined and thus a ballistic reflection scheme is not appropriate. Here we treat steric collisions by a rejection method similar to MC simulations. If a steric overlap between two clusters is created during a move step, this move step is rejected. One method to deal with this situation would be to repeatedly choose a new position of the two clusters, starting from their original location and orientation, until the move step is accepted. This method leads to incorrect simulation results as is demonstrated for the example of two hard spheres in a periodic box in Fig. 2. Here a histogram of the distance distribution between the two spheres, scaled by the volume of a spherical shell, is shown in a range in which boundary effects are not observed. By choosing a new position

until successful acceptance of the move step (green histogram), an effective repulsion between the two spheres is introduced, leading to a depletion zone at small particle distances instead of the expected uniform distribution. If, instead of choosing a new position, we set the two clusters involved in a steric collision back to their original position (and orientation) before the move step, we recover the expected uniform equilibrium distribution (shown in red in Fig. 2). Thus, this method ensures that the correct equilibrium distribution is realized.

D. Local rules

In our approach, clusters are rigid assemblies consisting of one or multiple proteins. Assuming that the assembly geometry is determined by unique local interactions, a set of local rules is necessary to describe the new relative orientation and position of two reacting clusters.[75] These local rules are encoded in the bond that is formed between the clusters. Each bond carries the information of the desired center-to-center (ctc) vector of the two proteins directly involved in the binding process as well as their relative orientation (torsion vectors). Upon reaction the two clusters instantaneously flip into the desired relative configuration. This rule follows from the assumption that the short-ranged forces involved in the final binding step lead to a fast rearrangement on the time scale of our BD simulation. The reorientation process is schematically shown in Fig. 1c. In a first step the clusters are shifted and rotated so that the predefined ctc-vector matches the real ctc-vector. This procedure enforces the correct position of the two merging clusters relative to each other. In a next step the relative orientation of the clusters is corrected by aligning the projection of the two torsion vectors on a plane perpendicular to the ctc-vector. The necessary rotation and translation of the clusters is distributed between them according to their diffusive weights. This means that for a small and a large partner, essentially only the small partner is moved, as one expects for physical reasons; for two similarly sized partners, both are moved to a similar extent. Since all interactions are local (e.g. local patches or constraints on orientation/torsion), the encounter complex corresponds to a region in configuration space surrounding the desired relative position and orientation. If this region is sufficiently small, the instantaneous flipping into the correct configuration is comparable to the resolution of the BD simulation. Reorientation of the clusters during the binding process can lead to a steric overlap either with another cluster or between the merging clusters. If this is the

case, the reaction is rejected and the old positions and orientations of the clusters before the move step are resumed. The steric collision of two merging clusters reflects that during the assembly process incompatible fragments can prevent the formation of the desired structure. For example if the desired structure encoded by the local bonds is a ring consisting of five proteins, two ring fragments each containing three proteins cannot bind with each other.

E. Microscopic and macroscopic rates

In order to implement full reversibility, both reaction directions are treated as stochastic reactions with two corresponding microscopic rates. If the reactive patches of two clusters form an encounter, specified by the constraints in Eq. 3 and Eq. 4, they can react with a bond-specific rate k'_a. Similarly an existing bond can dissociate with a bond-specific rate k'_d. Here we assume that the waiting times for association or dissociation of a bond between two clusters in encounter are Poisson-distributed, $P(t, k'_i) = k'_i \exp(-k'_i t)$, $i = \{a, d\}$. In this case the probability that no association or dissociation has occurred after a timestep Δt is given by $S(\Delta t, k'_i) = 1 - \int_0^{\Delta t} P(t, k'_i) dt$ and hence the probabilities for bond dissociation or bond formation are given by: [50]

$$P_{\text{assoc}} = 1 - S(\Delta t, k'_a) \approx k'_a \Delta t \ , \ P_{\text{dissoc}} = 1 - S(\Delta t, k'_d) \approx k'_d \Delta t. \tag{6}$$

The approximations used in Eq.6 are valid if $k'_d \Delta t \ll 1$ and $k'_a \Delta t \ll 1$, which is the case throughout this work.

We now show how the microscopic reaction rates k'_a and k'_d can be related to macroscopic reaction rates. In a macroscopic framework the reaction scheme in Eq. 2 can be interpreted as a system of ordinary differential equations describing the changes in the concentrations c_A,c_B,$c_{A\cdot B}$ and c_C of the different species involved in the reaction . [69] In this framework the encounter is understood as a single, intermediate state connecting the bound complex C and the unbound A and B particles. The encounter can either react to the final complex with the first order rate k_a or decay into two separated particles with the first order rate $k_{D,b}$. An encounter can be formed by the first order decay of cluster C with a rate k_d or by the diffusive association of an A and B particle described by the second order rate k_D. Here k_D has the dimension m^3/s if we consider particle concentrations in 3 dimensions. Using a steady state approximation of the encounter complex, the following relations are obtained

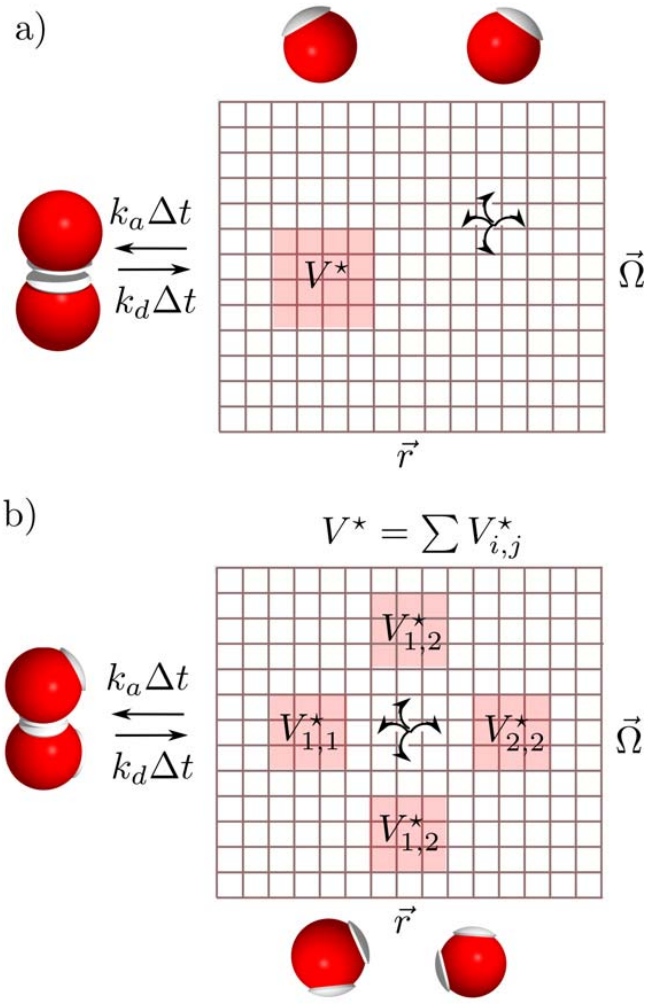

FIG. 3. Illustration of the reactive volume $V^\star$. The configuration space is defined by the relative position $\vec{r}$ of the particles and the 2×3 dimensional orientation vector $\vec{\Omega}$. a) In the case of one reactive patch $V^\star$ corresponds to the region in configuration space in which two particles are considered to be in encounter (Eq. 3 and Eq. 4). b) For particles with multiple reactive patches different regions $V^\star_{i,j}$ in configuration space correspond to an encounter mediated by one particular patch combination i,j. For identical microscopic rates k_a and non-overlapping $V^\star_{i,j}$ the total reactive volume $V^\star$ between the two particles is given by the sum over the encounter volumes associated with each patch combination.

for the overall forward and backward rates and the equilibrium constant [69]:

$$k_+ = \frac{k_D k_a}{k_a + k_{D,b}} \ , \ k_- = \frac{k_{D,b} k_d}{k_a + k_{D,b}} \tag{7}$$

$$\Rightarrow K_{\text{eq}} = \frac{k_+}{k_-} = \frac{k_D}{k_{D,b}} \frac{k_a}{k_d}. \tag{8}$$

In the case of a diffusion-limited reaction $k_a \gg k_{D,b}$. [69] In this case the overall forward and reverse rates simplify into the purely diffusion-limited forward rate $k_+ \approx k_D$ and the backward rate k_- becomes $k_- \approx k_{D,b} k_d / k_a$. In the case that the reaction is reaction-limited ($k_{D,b} \gg k_a$), the overall forward rate becomes $k_+ \approx k_D k_a / k_{D,b}$ and the overall backward rate is $k_- \approx k_d$.

In the framework of the Fokker-Planck equation two spherical particles are considered to be in an encounter if they are in contact. [27, 28] Finite reactivity for particles in encounter was introduced by Collins and Kimball [28] in the form of a radiation boundary condition in which the rate κ_a (termed κ in Ref. [70] and k in Ref. [28]) relates the concentration at contact to the reactive flux. By comparing the escape probabilities from the encounter in the Fokker-Planck framework and the macroscopic rate equation framework, Shoup and Szabo showed that κ_a can be related to macroscopic rates by identifying $\kappa_a = k_D k_a / k_{D,b}$ and $K_{\text{eq}} = \kappa_a / k_d$. [70] Agmon and Szabo derived the same relation for the equilibrium constant ($K_{\text{eq}} = \kappa_a / k_d$) by considering an isolated pair of reactive spheres using a back-reaction boundary condition. [36]

Here we show how the microscopic reaction rate used to describe reactions in our simulation approach can be related to the reaction scheme in Eq. 2 and to the equilibrium constant (Eq. 8). Inspired by the work of Shoup and Szabo [70] we calculate the equilibrium constant for the formation of the encounter. In our approach the encounter is defined as a region in configuration space (Eq. 3 and Eq. 4) around the desired relative position in the bound complex instead of a boundary as commonly used in the Fokker-Planck picture. The configuration space of two rigid unbound particles in a periodic box of volume V can be described by their relative position vector $\vec{r}$, their center-of-mass vector $\vec{R}$ and 2×3 angular coordinates $\vec{\omega}_1$ and $\vec{\omega}_2$. Assuming free diffusive motion without reactions all configurations in the two particle configuration space are equally probable and they only interact by steric repulsion. By using the thermodynamic extremum principle for the Gibbs free energy, we can relate the equilibrium constant for the formation of an encounter to the partition sums of the free molecules z_A and z_B and to the partition sum of the encounter complex $z_{A \cdot B}$

[44, 76]:

$$K_{\mathrm{eq}}^{\mathrm{enc}} = \frac{k_D}{k_{D,b}} = \frac{(z_{A\cdot B}/V)}{(z_A/V)(z_B/V)} \tag{9}$$

$$z_A = z_B = \int_V d^3x \int d^3\omega = V \times 4\pi \times 2\pi \tag{10}$$

$$z_{A\cdot B} = \int_V d^3R \int d^3r \prod_{i=1}^{2} \left(\int d^3\omega_i \right) \tag{11}$$

$$\Rightarrow K_{\mathrm{eq}}^{\mathrm{enc}} = \int d^3r \prod_{i=1}^{2} \left(\frac{1}{8\pi^2} \int d^3\omega_i \right) =: V^\star. \tag{12}$$

For the single molecules all positions and orientations (neglecting the excluded volume) are accessible, resulting in a factor of V from the integration over the translational degrees of freedom and a factor of $8\pi^2$ from the orientational degrees of freedom of the rigid molecules. To determine the partition sum of the encounter complex $z_{A\cdot B}$, we first integrate out the center-of-mass coordinate $\vec{R}$ of the two molecules resulting in a factor of V. The boundaries of the remaining integrals over the relative position coordinate $\vec{r}$ and the orientation coordinates $\vec{\omega}_1$ and $\vec{\omega}_2$ are determined by the patch definition and the particle geometries. They follow from Eq. 3 and Eq. 4 and have to be calculated for every specific case, as will be discussed in more detail below. The resulting reactive volume $V^\star$ is the central concept to relate microscopic and macroscopic rates. From Eq. 12 we see that it equals the equilibrium constant $K_{\mathrm{eq}}^{\mathrm{enc}}$.

If we now allow for reactions, not every configuration in the encounter region is equally populated as some particles will already react before they explore the inner region of $V^\star$. However, if on average the encounter region is well explored before an association, we can approximate the real distribution within $V^\star$ by a uniform distribution. This approximation is equivalent to the underlying assumption in the work of Pogson et al [77] and Klann et al. [78] who introduced a reactive volume (and an intrinsic association rate [78]) based on the assumption that the particles are randomly distributed in the box at all times.

Alsallaq and Zhou also used thermodynamic arguments to determine the equilibrium constant for the bound complex. [44] However, in contrast to this work we consider all configurations within the generalized reactive volume $V^\star$ as encounter configurations. By introducing finite reactivity with the microscopic reaction rate k_a' with which a bound complex can be formed from the encounter region (see Fig. 3a), our approach can account for reactions which are reaction- or diffusion-limited, as will be shown below in the results

section. To study assembly, this is of great importance as intermediates emerging during the assembly process can have very different diffusion properties and a reaction that was reaction-limited for small clusters can become diffusion-limited for larger clusters.

Thus, by identifying the equilibrium constant for the formation of the encounter with the reactive volume $V^\star$ (Eq. 12) and relegating bond association and dissociation to the reaction rates, we can identify the reaction rates k'_a and k'_d in the microscopic framework with the corresponding reaction rates k_a and k_d in the macroscopic framework (Eq. 8) and the equilibrium constant is given by:

$$K_{\text{eq}} = \frac{k_D}{k_{D,b}} \frac{k_a}{k_d} = V^\star k_a / k_d \ . \tag{13}$$

In accordance with the work by Shoup and Szabo [70] the rate $\kappa_a = V^\star k_a$ is given by the product of the equilibrium constant for the formation of the encounter complex and the reaction rate for the formation of the final complex. This rate can be identified with the reaction rate used by Morelli and ten Wolde [50] (k_a in ref. [50]).

While the reactive volume $V^\star = k_D/k_{D,b}$ is sufficient to predict the correct equilibrium constant (Eq. 13), the kinetics of the reactions depend on the absolute values of the diffusive rates k_D and $k_{D,b}$. Thus in order to determine the macroscopic rates k_+ and k_- defined in Eq. 7, we need to evaluate k_D. This can be done within our simulation approach based on an algorithm by Zhou [39]. In this algorithm k_D can be calculated from the survival probability $S(t)$ of two particles starting in encounter by [39, 43]:

$$k_D = \lim_{t\to\infty} \kappa_a \frac{S(t)}{1 - S(t)}. \tag{14}$$

Given the diffusive on-rate k_D, the diffusive off-rate $k_{D,b}$ can be simply calculated by $k_{D,b} = k_D/V^\star$ (Eq. 9).

Any simulation algorithm with underlying reversible dynamics needs to satisfy detailed balance. To establish detailed balance we follow the approach by Morelli and ten Wolde [50] who inferred from a detailed balance consideration that the relative position distribution of two spherical particles prior to a reaction has to be identical (after renormalization) to the position distribution of the two particles after dissociation. For two hard spheres covered with a reactive shell, it has been argued that detailed balance can be introduced by placing the two hard spheres according to a radial uniform distribution within the reactive shell followed by one additional move step [79]. Here we generalize this idea as follows:

Upon the dissociation of two clusters, a new configuration is chosen uniformly within the encounter region $V^\star$ followed by a diffusive move step of the two clusters. To establish the uniform distribution in $V^\star$ we exploit the time invariance symmetry of the diffusion propagator. This symmetry ensures that in a confined volume of the configuration space a uniform distribution is established as the steady state distribution. As $V^\star$ describes a configuration around the desired relative configuration of the proteins, we can generate a uniform distribution without prior knowledge of the exact shape of the reactive volume by performing various "pseudo-diffusion" steps of the two clusters starting from their predefined relative configuration. These "pseudo-diffusion" steps are confined to the region $V^\star$ in the relative accessible configuration space of the two partners. We call this procedure "pseudo-diffusion" as the two dissociating clusters are propagated diffusively within $V^\star$, however, the timestep used to establish the uniform distribution has no physical meaning. This procedure for generating a uniform distribution within the reactive area does not depend on the particle or patch geometry. Thus it is especially suited to study assembly dynamics as parts of the reactive volume might become sterically blocked during the assembly process. These steric effects are automatically taken into account with our method. The effect of steric blocking and its consequences for assembly will be discussed in the results section. Moreover, this method would also remain valid when including long range electrostatic interactions. In this case the distribution within the encounter complex in equilibrium would not be uniform. However, the "pseudo-diffusive" motion step would lead to the expected distribution within $V^\star$.

In general the encounter volume $V^\star$ has to be understood as the volume of all two particle configurations resulting in an encounter between two clusters (see Fig. 3b). This means that for clusters with multiple patches the total encounter volume $V^\star = \bigcup V^\star_{p_i,p_j}$ where $V^\star_{p_i,p_j}$ is the encounter volume between a pair of patches. In the case of a dissociation of clusters with multiple patches a uniform configuration in the subvolume $V^\star_{p_i,p_j}$ of the patches that formed the bond is realized. If the different patches have a different microscopic reactivity, the subvolumes have to be treated separately and the equilibrium constant for the complex formation is given by the sum of the different equilibrium constants for different bonds.

F. Intrinsic association

Proteins with multiple reactive patches can assemble in structures containing loops. In this case an already connected cluster can contain open bonds with two patches being in permanent encounter due to the geometry of the cluster. These patches can bind with the internal association rate k_a^{intra}, where we again assume Poisson-distributed waiting times for the bond formation. The bond formation in this case is fundamentally different from the above discussed process as no diffusion is involved. Since clusters are rigid objects, internal bond formation does not change the shape of the cluster. Thus it can be considered as an internal process stabilizing an already existing structure. Given a dissociation rate of k_d for a specific bond, we can relate the internal association rate to the free energy E of bond formation. For a closed loop containing n bonds, there are n different configurations with one open bond in the loop and the fraction of the open and closed loop in equilibrium is given by:

$$\frac{p_{\text{open}}}{p_{\text{closed}}} = \frac{nk_d}{k_a^{\text{intra}}} = \frac{Z_{\text{open}}}{Z_{\text{closed}}} = \frac{n}{e^{-\beta E}} \Rightarrow k_a^{\text{intra}} = k_d e^{-\beta E}. \tag{15}$$

Thus, the internal association regulates the fraction of open and closed loop configurations. In a more realistic scenario, the dissociation of one bond in a loop will enable an enhanced internal movement. This will be reflected in an increase in the entropy which would shift the ratio of open and closed ring structures towards the open state (smaller k_a^{intra}). In principle it should be possible to calculate the change in energy and entropy upon dissociation of a bond using detailed MD simulations. Such simulations could be used to specify the internal association rate.

G. Outline of the algorithm

In this part we will describe the work flow of our algorithm. Once a starting configuration is seeded the following steps are repeated iteratively. Firstly every particle is translated and rotated according to its diffusive properties in the framework of free Brownian motion within a timestep Δt. With the new positions and orientations all clusters with steric overlaps as well as all clusters participating in a reaction are tagged. A reaction between two clusters occurs with the bond specific probability $k_a \Delta t$ if they are in encounter. In a next step all steric overlaps (including box overlaps if the box is non-periodic) are corrected by setting

the involved particles back to their original position before the move step. This might lead to further steric overlaps as a higher order effect. These overlaps are then also corrected. In this step clusters tagged for a reaction click into their predefined relative positions and orientations (see Fig. 1c). If a reaction leads to a steric overlap either between the two merging clusters or with other clusters, the reaction is rejected and the particles reassume their configuration before the move step. Collisions with other clusters after the reorientations step is a higher order effect in the concentration of the particles. In dilute systems, especially for reactive configuration volumes around the desired relative configuration, this happens rarely. In a next step open, internal bonds can be closed with probability $P_{\text{intra}}^{\text{acc}} = k_a^{\text{intra}} \Delta t$. Finally each existing bond can dissociate with the bond specific probability $k_d \Delta t$. If this leads to two unconnected cluster fragments, the diffusive properties of the fragments are calculated. Subsequently a uniform distribution within the encounter volume $V^\star$ is realized by "pseudo-diffusive" motion preserving the encounter followed by one unconstrained diffusion step of the two clusters. All simulations have been performed at room temperature $T = 293K$ and with the viscosity of water $\eta = 1\text{mPas}$.

III. RESULTS AND DISCUSSION

A. The reactive volume

As discussed in the previous section, we can relate the microscopic rates to the macroscopic equilibrium constant using the concept of a generalized reactive volume $V^\star$ in configuration space (Eq. 13). Here we introduce a model system in which it is possible to analytically calculate $V^\star$ and show that the results from our MC scheme (Eq. 17) agree well with the analytical results. In this model system a protein is described by one hard sphere of radius R equipped with one polar patch as depicted in Fig. 3a. The patch is centered at the origin of the protein. It has a radius of R_p and an opening angle of $\theta_p \in [0, \pi]$ around the z-axis of the proteins. With our definition of the encounter complex for two such particles (Eq. 3 and Eq. 4), we can analytically calculate $V^\star$ by decomposing the radial and

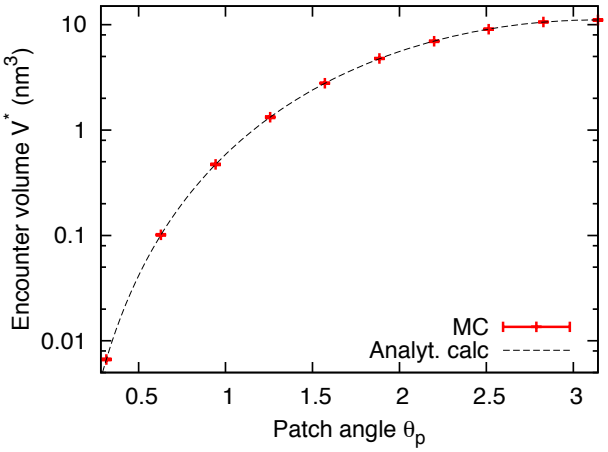

FIG. 4. $V^\star$ for two identical hard spheres of radius $R = 1$nm equipped with one polar patch of radius $R_p = 1.1$nm as a function of the patch angle θ_p. The analytical result from Eq. 16 is shown with a dashed line while the MC estimates (according to Eq. 17) are represented by red points with error bars.

orientational part, similar to the potential model proposed by Kern and Frenkel[80]:

$$V^\star = V^\star_{\text{rad}} \times V^\star_{\text{ori}} \tag{16}$$
$$V^\star_{\text{rad}} = \frac{4}{3}\pi((R^p)^3 - R^3),\ V^\star_{\text{ori}} = \left(\frac{1}{4\pi}\int_0^{2\pi} d\phi \int_0^{\theta_p} \sin(\theta) d\theta\right)^2 = \frac{1}{4}(1-\cos(\theta_p))^2.$$

The square in the orientation part arises from the fact that we have to consider two independently rotating particles and only if the orientation of both particles is correct, an encounter is reached (see Eq. 4). For $\theta_p = \pi$ the orientation constraint vanishes and the spherical result is recovered.

As analytically calculating the reactive volume is only feasible for some special geometries, it can be numerically pre-calculated for the elementary assembly blocks using a MC integration scheme. In this scheme we sample different configurations by randomly positioning two clusters with random orientations in a periodic box of volume V_{box}. We repeat this procedure N times and can estimate $V^\star$ by counting the fraction of trials $n = N_{\text{encounter}}/N_{\text{total}}$ that result in an encounter configuration. Then we simply have

$$V^\star_{MC} = nV_{\text{box}}. \tag{17}$$

In Fig. 4 the configuration space volume $V^\star$ for two identical, spherical proteins equipped with a polar patch ($R = 1$nm and $R_p = 1.1$nm) is shown as a function of the opening

angle θ_p. Comparing the analytical result (black line) and MC simulation (Eq. 17) we see that our simple MC scheme correctly estimates $V^\star$. For proteins equipped with multiple, non-overlapping patches which can bind with each other via different patch combinations, we have to distinguish between the encounter volume $V^\star_{p_i,p_j}$ of two specific patches p_i and p_j and the total encounter volume $V^\star$ of two proteins. The total configuration volume $V^\star$ is given by the union of all volumes $V^\star_{p_i,p_j}$ for the encounter of two different patches i,j that can bind to each other. If the encounter volumes of different patch combinations are disjoint, the total configuration space volume for the encounter of two clusters is given by summing over all $V^\star_{p_i,p_j}$. For multiple, identical patches that can bind with each other, the total reactive volume $V^\star$ is given by multiplying the configuration volume $V^\star_{p_i,p_j}$ of one patch combination with a combinatorial prefactor accounting for the multiplicity of the different patch configurations if the corresponding volumes are not overlapping in configuration space.

B. Bimolecular reactions

To verify our algorithm and to show the importance of detailed balance, we first analyze a system with a small number of proteins only. In detail we consider a situation in which one particle of type A and N_B particles of type B are placed in a periodic box of volume V_{box}. In this case we can relate the concentration c_C of the complex C to the fraction of time t_b in which particle A is bound to particle B ($p_b = t_b/(t_u + t_b)$), while the concentration c_A of particle A can be related to the fraction of time t_u in which A is unbound ($p_b = t_u/(t_u + t_b)$). The unbound A particle is surrounded by a concentration of $c_B = N_B/V$ particles of type B. Here $V = V_{\text{box}} - V_{\text{excl}}$ is the freely accessible volume. For proteins of identical radius ($R_A = R_B = R$) the excluded volume can be approximated by $V_{\text{exc}} = 4\pi N_B (2R)^3/3$. Thus we can relate the probability that A is bound to the equilibrium constant of the reaction by: [36, 50]

$$K_{\text{eq}} = \frac{c_C}{c_B c_A} = \frac{p_{\text{bound}}}{\frac{N_B}{V}\left(1 - p_{\text{bound}}\right)} \Rightarrow p_{\text{bound}}(N_B) = \frac{K_{\text{eq}} N_B}{K_{\text{eq}} N_B + V}. \tag{18}$$

Eq. 18 follows from elementary thermodynamic arguments and is valid irrespective of the details of the binding interactions. In the following subsections we will show that the correct equilibrium bound probability is reproduced with our algorithm for spherically reactive and patchy particles when appropriately taking the generalized encounter volume $V^\star$ into

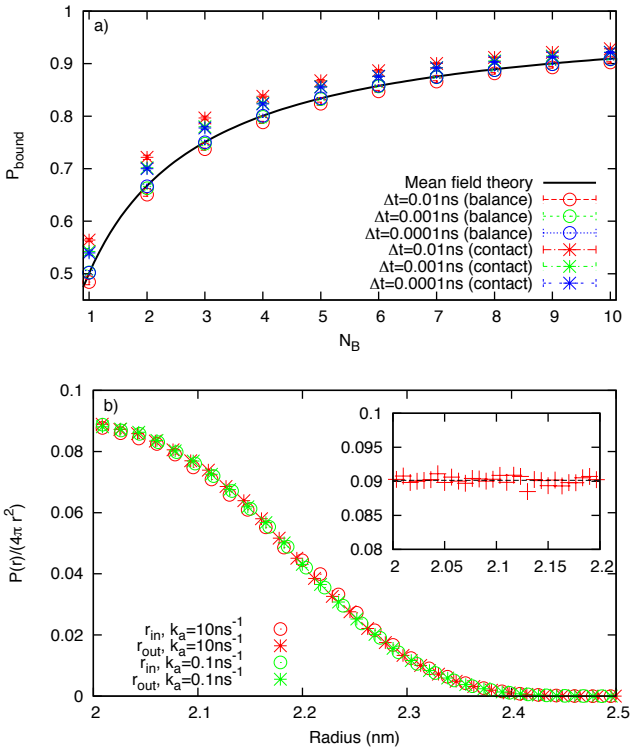

FIG. 5. Equilibrium bound probabilities and radial distribution for spherically reactive particles. a) The probability of one A particle being bound to a B particle is shown as a function of the number of B particles according to Eq. 18 (black line) for $K_{\mathrm{eq}} = V_{\mathrm{box}}$. The following parameters have been used for the simulations: $R_A = R_B = 1\mathrm{nm}$, $R_{p,A} = R_{p,B} = 1.1\mathrm{nm}$, $\theta_{p,A} = \theta_{p,B} = \pi$ leading to $V^\star \approx= 11.09\mathrm{nm}^3$ (Eq. 16). For a given $k_a = 10\mathrm{ns}^{-1}$, the dissociation rate k_d is chosen so that $V^\star \frac{k_a}{k_d} = V_{\mathrm{box}} = 8000\mathrm{nm}^3$ (Eq. 13). Circles depict the simulation results obtained with our algorithm for different time resolutions while stars correspond to simulations in which detailed balance is violated by placing particles in contact after dissociation. b) The normalized radial distribution Δt before reaction (circles) and after dissociation including the additional unconstrained move step (stars) is shown for two different association rates $k_a = 10\mathrm{ns}^{-1}$ (red) and $k_a = 0.1\mathrm{ns}^{-1}$(green) with a time resolution of $\Delta t = 0.01\mathrm{ns}$. The inset shows the comparison of the uniform radial distribution established by "pseudo-diffusive" motion constraint to $V^\star$ (red points) and the expected uniform distribution in a spherical shell (black line).

account. We also show that detailed balance is essential to reproduce p_{bound} from Eq. 18.

1. *Spherically reactive particles*

Here we compare our BD algorithm with the mean field result (Eq. 18) for the case of spherically reactive A and B particles ($R_A = R_B = 1\text{nm}$, $R_{p,A} = R_{p,B} = 1.1\text{nm}$, $\theta_{p,A} = \theta_{p,B} = \pi$, $V^\star = 11.09\text{nm}^3$) and show that our algorithm fulfills detailed balance in this case. Given an association rate of $k_a = 10\text{ns}^{-1}$ we chose k_d so that $K_{\text{eq}} = V^\star \frac{k_a}{k_d} = V$. In Fig. 5a the probability of particle A being bound to particle B is shown as a function of the number of B particles N_B and compared to the mean field result (black line). Placing particles uniformly in the reactive shell by "pseudo-diffusive" motion and allowing for one unconstrained move step of the two proteins involved in the dissociation according to the algorithm described above (circles) leads to very good agreement between the mean field theory and the simulation results. Only for a very large timestep $\Delta t = 0.01\text{ns}$ leading to a large reaction probability of 0.1 a small deviation between the simulation results and the expected mean field theory is observed. On the contrary, violating detailed balance by placing particles in contact after the dissociation (stars) leads to an overestimation of p_{bound} and the simulation results cannot be reconciled with the mean field theory. Although reducing the timestep from $\Delta t = 0.01\text{ns}$ to $\Delta t = 0.001\text{ns}$ leads to a modest improvement for the simulation results with contact dissociation, no further improvement is observed when decreasing the timestep further. This shows that detailed balance is essential in the dissociation step for the agreement between simulation results and macroscopic theory. These findings agree with those obtained by Morelli and ten Wolde who performed a similar simulation to test their algorithm. [50]

In Fig. 5b we verify that our algorithm indeed obeys detailed balance by comparing the radial distribution of particles before a reaction (circles) and after dissociation (stars) for two different association rates. Irrespective of the choice of k_a we observe the same radial distribution before reaction and after dissociation and thus our algorithm satisfies detailed balance for this quasi one-dimensional case. In the inset of Fig. 5b we show a histogram of the distance between two dissociating particles after the "pseudo-diffusive" motion constraint to $V^\star$ without the additional, unconstrained move step of the two particles. Here we see that we are indeed able to generate a uniform distribution within $V^\star$ by exploiting the symmetry

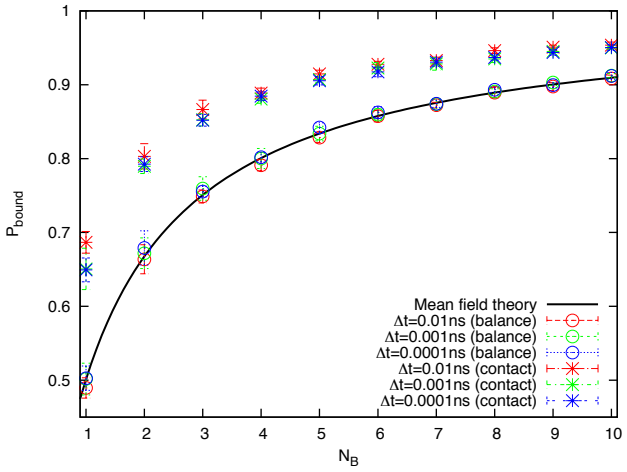

FIG. 6. Equilibrium bound probabilities for patchy particles. The probability of one A particle being bound to a B particle is shown as a function of the number of B particles according to Eq. 18 (black line) for $K_{\text{eq}} = V_{\text{box}}$. The mean field theory is independent of the specific particle details. The following parameters have been used for the simulations: $R_A = R_B = 1\text{nm}$,$R_{p,A} = R_{p,B} = 1.1\text{nm}$, $\theta_{p,A} = \theta_{p,B} = \pi/4$ leading to $V^\star \approx= 0.23\text{nm}^3$ (Eq. 16). For a given $k_a = 10\text{ns}^{-1}$ the dissociation rate k_d is chosen so that $V^\star \frac{k_a}{k_d} = V_{\text{box}} = 8000\text{nm}^3$. Circles show the results of our algorithm for various timesteps while stars correspond to simulations in which detailed balance is violated by placing particles in contact and with perfect alignment of the patches after dissociation.

of the diffusion propagator as the histogram of the simulated positions agrees very well with the expected uniform distribution.

2. Patchy Particles

After verifying that our algorithm reproduces the expected results for spherically reactive particles, we will now investigate the effect of anisotropic reactivity and show that our generalized definition of the reactive volume enables us to compare our simulation results with the mean field theory, which is the same as for spherically reactive particles. Here we consider the same setup as in the previous part with one particle of type A and N_B particles of type B in a periodic box ($R_A = R_B = 1\text{nm}$ and $R_{p,A} = R_{p,B} = 1.1\text{nm}$). This time, however, both particles are equipped with a polar patch ($\theta_p = \pi/4$) allowing only for an association of two particles if the patches are sufficiently aligned with the ctc-vector of the

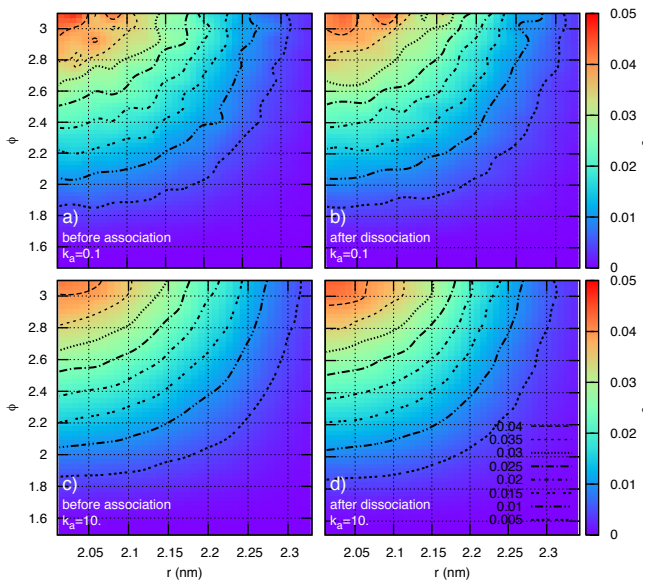

FIG. 7. Color-coded histogram of the particle positions before reaction and after dissociation as a function of the relative distance r and the angle between the orientations of the two patches ϕ. This histogram has been weighted by the generalized bin volume $(4\pi r^2 dr \times 2\pi \sin(\phi) d\phi)$. Several contour lines are shown for better comparability. In a) and c) the distribution of particle positions before a reaction is shown for $k_a = 0.1\text{ns}^{-1}$ and $k_a = 10\text{ns}^{-1}$, respectively. In b) and d) the corresponding distributions of particle positions after dissociation is shown. The distributions have been recorded with a timestep resolution of $\Delta t = 0.01\text{ns}$.

proteins (Eq. 4). In this case the reactive volume reduces to $V^\star = 0.23\text{nm}^3$ according to Eq. 16. Given the reactive volume $V^\star$ and the association rate $k_a = 10\text{ns}^{-1}$, we again choose k_d in such a way that $K_{\text{eq}} = V$. The comparison between the simulation and mean field theory is shown in Fig. 6. By using the appropriate scaling with the generalized volume $V^\star$ for the patchy particles, we observe perfect agreement of the mean field results from Eq. 18 (black line) with the simulation results when placing the particles according to the proposed detailed balance algorithm (circles). When placing the particles in contact (alignment of patch orientation with ctc-vector and radial contact), we drastically overestimate the bound probability (stars). Compared to the spherical case (Fig. 5) this overestimation of p_{bound} is much stronger. Thus, in the case of localized reactivity it is even more important to carefully consider the relative position and orientation of dissociating proteins. Moreover our results confirm the relation between microscopic rates and the macroscopic equilibrium constant

given in Eq. 13.

In Fig. 7 we again show the distribution of the relative position and orientation of two particles equipped with a polar patch before a reaction and after dissociation. Here ϕ corresponds to the angle between the orientation vectors of the patches and r is the distance between the centers of the two particles. Due to the symmetry of the particles around the z-axis these two parameters provide a good description of the relevant configuration space. The normalized probability distribution $p(r,\phi)/(4\pi r^2 \times 2\pi sin(\phi))$ is shown color-coded for two microscopic association rates $k_a = 0.1\text{ns}^{-1}$ (Fig. 7 upper part) and $k_a = 10\text{ns}^{-1}$ (Fig. 7 lower part) at a time resolution of $\Delta t = 0.01\text{ns}^{-1}$. In the left part of Fig. 7 the distribution before reaction is shown while in the right part the corresponding distribution after dissociation is depicted. As expected the distribution has its maximum for particles in contact and anti-parallel aligned patch orientations ($r = 2.0$nm and $\phi = \pi$). Although the distributions fluctuate more for a smaller association constant (Fig. 7a and 7b), as can be seen by looking at the contour lines, very good agreement between the distribution before association and after dissociation is observed for both association parameters. This shows that our algorithm maintains detailed balance in this case of non-spherical reactivity. Changing the association rate by two orders in magnitude does not affect the distributions suggesting that our algorithm works well for a large spectrum of microscopic parameters. This first example of non-spherically reactive particles shows that it is essential to appropriately scale the macroscopic parameters using the concept of a generalized reactive volume in configuration space. Moreover, careful consideration of the relative position and orientation of the dissociating particle is necessary to obtain quantitative agreement between BD simulations and mean field theory or experimental results.

C. Beyond bimolecular reaction: Assembly of a pentameric ring

In this section we analyze the assembly of a pentameric ring structure consisting of 5 proteins (Fig. 8b) as an example of an assembly process involving more than two partners. As elementary building blocks we consider spherical proteins of radius $R = 1$nm, each equipped with two reactive patches (Fig. 8a). The patches are centered at the origin of the protein and both have a radius of of $R_p = 1.1$nm and an opening angle of $\theta_p = \pi/5$. The geometry of the ring is reflected in the different orientation vectors $\vec{\sigma}$ associated with each

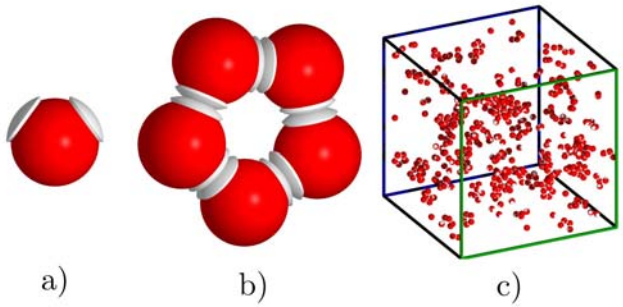

FIG. 8. Simulation of the assembly of a pentameric ring structure. a) Elementary spherical building block of radius $R = 1$nm for the pentameric ring equipped with two patches. The angle between the centers of the patches is determined by the desired ring structure. Each patch has an opening angle of $\theta_p = \pi/5$ and a radius of $R_p = 1.1$nm. b) Fully assembled ring structure. c) Simulation snapshot of a typical box containing 500 proteins.

patch, and the relative position and orientation of the proteins are encoded in the bond structure.

Here we develop a rate equation approach based on a set of ordinary differential equations (ODEs) to describe the changes in concentration of the different fragments sizes. We demonstrate how the macroscopic reaction rates can be calculated from the microscopic reaction parameters and diffusive properties of the intermediates. The parameter free comparison of our simulation results with the rate equation predictions shows excellent agreement. This demonstrates that we are indeed able to predict macroscopic reaction rates from our simulations taking into account changes in diffusive properties of the assembly intermediates as well as steric effects arising during the assembly process.

1. Macroscopic rates

In Eq. 7 the reaction rates k_+ and k_- are given in the case of a bimolecular reaction. We now specify the macroscopic rates $k_+^{i,j}$ and $k_-^{i,j}$ for the reaction between two ring fragments

Size	1	2	3	4
1	0.40	0.40	0.40	0.24
2	0.40	0.40	0.36	-
3	0.40	0.36	-	-
4	0.24	-	-	-

TABLE I. Generalized reactive volumes $V^{\star}_{i,j}$ in nm^3 for the encounter of different ring fragments calculated by MC sampling according to Eq. 17 and analytically according to Eq. 16 for $V^{\star}_{1,1}$, respectively.

Size	1	2	3	4
1	3.29	2.69	2.15	1.17
2	2.69	2.03	1.52	-
3	2.15	1.52	-	-
4	1.17	-	-	-

TABLE II. Diffusive on-rates k_D for different ring fragments in nm^3/ns. The rates have been calculated from the survival probabilities of fragments starting in a encounter according to the algorithm proposed by Zhou[39] with a minimum timestep resolution of $\Delta t = 0.01$ns.

with i and j proteins. These rates are given by:

$$k_+^{i,j} = \overbrace{\frac{k_D^{i,j} k_a}{k_{D,b}^{i,j} + k_a}}^{\tilde{k}_+^{i,j}} (1 - \frac{1}{2}\delta_{i,j}) \tag{19}$$

$$k_-^{i,j} = \underbrace{\frac{k_{D,b}^{i,j} kd}{k_{D,b}^{i,j} + k_a}}_{\tilde{k}_-^{i,j}} (2 - \delta_{i,j}). \tag{20}$$

$k_+^{i,j}$ describes the association of two ring fragments of size i and j. As the diffusive properties and the accessible reaction volume change with the size of the fragments $k_+^{i,j}$ is different for different combination of fragments, albeit the microscopic reaction rate k_a remains constant. For the reaction of identical particles the macroscopic rate is reduced by a prefactor of 1/2 compared to the simulation rate k_a. This reflects the fact that for reactions of identical components ($A + A \rightarrow C$) the observed macroscopic rate is by a factor of 1/2 smaller

than the rate used in the simulation due to the number of collisions being proportional to $N_A(N_A-1)/2!$. [47, 52] $k_-^{i,j}$ describes the macroscopic dissociation rate of a cluster of size $i+j$ into two ring fragments of size i and j, respectively. To determine the macroscopic reaction rates given in Eq. 19 and Eq. 20 we need to calculate the diffusive on- and off-rates $k_D^{i,j}$ and $k_{D,b}^{i,j} = k_D^{i,j}/V_{i,j}^\star$ which change for different combination of fragments. Here $V_{i,j}^\star$ is the configuration volume associated with the reaction of two fragments of size i and j.

The reactive volume for two different fragment configurations i and j can be calculated by MC sampling as has been described in Eq. 17. The resulting volumes $V_{i,j}^\star$ for two fragments of size i and j are shown in Table I. For the reaction of two monomers the reactive volume $V_{1,1}^\star$ can also be evaluated by using Eq. 16 for the encounter of one specific pair of patches. Taking into account the multiplicity of bond interactions 2^2 results in a total encounter volume of $V_{11}^\star = 0.4\text{nm}^3$. While fragments not combining into a full ring ($i+j<5$) have the same configuration volume as the monomeric fragments, the configuration volume for fragments that can combine into a full ring is reduced. This reflects the fact that, independent of the particle geometry, the encounter volume and thus the number of configurations in this volume remains unchanged, unless parts of the reactive volume become sterically blocked, which is the case for fragments that can assemble into the full ring structure. Moreover, for these fragments some configurations with a simultaneous overlap of different patch combinations exist. As the encounter volumes for different patch combinations are not disjoint in this case, the total encounter volume is smaller than the sum of the subvolumes. These effects are naturally included in our simulation algorithm and for the simulations only knowledge of the reduced volume for the basic building blocks $V_{1,1}^\star$ is required. However, in order to compare our simulation results to a macroscopic rate equation approach, we need to determine the changes in the encounter volumes for different assembly intermediates.

Moreover, in order to capture the reaction kinetics with the above defined rates, we need to determine the diffusive on-rates $k_D^{i,j}$. In order to calculate the diffusive on-rate $k_D^{i,j}$ we follow a scheme which was originally proposed by Zhou. [39]. Here, two ring fragments of size i and j are initially placed in a random configuration in encounter (e.g. a random configuration within $V_{i,j}^\star$ is chosen). Starting from this configuration the two fragments are propagated diffusively within our simulation framework. If the two fragments form an encounter, they can react with the probability $k_a\Delta t$. In this case the run is terminated. By recording the survival probability $S^{i,j}(t)$ (the fraction of runs which survive until time t) $k_D^{i,j}$

can be estimated according to Eq. 14 with $\kappa_a^{i,j} = k_a V_{i,j}^\star$. In order to calculate $S^{i,j}(t \to \infty)$ we use a microscopic reaction rate of $k_a = 1\text{ns}^{-1}$ and an adaptive timestep scheme with a minimum timestep of $\Delta t_{\min} = 0.01\text{ns}$ which ensures that all steric collision and encounters are detected on the resolution of the minimum timestep. [39] The diffusive off-rate for the decay of a fragment into two smaller fragments of size i and j is given by $k_{D,b}^{i,j} = k_D^{i,j}/V_{i,j}^\star$. The absolute values for the different ring fragments are given in Tab. II. As fragments with $(i + j) > 5$ cannot combine with each other due to steric collisions, the diffusive on-rate in this case is $k_D^{i,j} = 0$.

2. Macroscopic rate equation approach

After having defined the macroscopic reaction rates for the association and dissociation of different ring fragments (Eq. 19 and Eq. 20) we will now introduce a system of ODEs to describe the changes in concentration c_i of a ring fragment of size i. This description assumes that the system is homogeneous and well mixed at all times. Stochastic fluctuations arising from the finite number of proteins are neglected. While for ring fragments containing less than 5 proteins only one state exists, two states exist for the full ring: an open ring with 4 bonds and a closed ring with 5 bonds. The closed ring can be considered as an internal state as the last bond formation in our framework does not involve any diffusion and it is connected to the open state by the internal association rate k_a^{intra} (see Eq. 15). The concentration of the open state is denoted by c_5 while the concentration of the closed state is denoted by $c_5^\star$. The changes in concentration for a ring consisting of N proteins can be described by the following set of ODEs:

$$\dot{c}_i = -\sum_{l=1}^{N-i} k_+^{i,l}(1+\delta_{i,l})c_i c_l - \sum_{\substack{l=1 \\ l\leq i-l}}^{i-1} k_-^{l,i-l} c_i - k_a^{\text{intra}}\delta_{i,N}c_N$$
$$+ \sum_{\substack{l=1 \\ l\leq i-l}}^{i-1} k_+^{l,i-l} c_l c_{i-l} + \sum_{l=1}^{N-i} k_-^{i,l}(1+\delta_{i,l})c_{l+i} + N\delta_{i,N}k_d c_N^\star \tag{21}$$
$$= -\sum_{l=1}^{N-i} \tilde{k}_+^{i,l} c_i c_l - \sum_{l=1}^{i-1} \tilde{k}_-^{l,i-l} c_i - k_a^{\text{intra}}\delta_{i,N}c_N$$
$$+ \frac{1}{2}\sum_{l=1}^{i-1} \tilde{k}_+^{l,i-l} c_l c_{i-l} + 2\sum_{l=1}^{N-i} \tilde{k}_-^{i,l} c_{l+i} + N\delta_{i,N}k_d c_N^\star \tag{22}$$
$$\dot{c}_N^\star = -Nk_d c_N^\star + k_a^{\text{intra}} c_N. \tag{23}$$

In our case $N = 5$. Eq. 21 shows the different processes which lead to a change in the concentration of a fragment containing i proteins. The first three terms lead to a decrease in concentration. The first term describes the change in concentration due to the reaction of a fragment of size i with another fragment of size l. If $i = l$ a twofold decrease in concentration c_i is observed. The second term describes the change in concentration due to the decay of a fragment of size i into two fragments of size l and $i - l$. To prevent the double counting of dissociation events the constraint $l \leq i - l$ for the summation is used here. In the third term the internal bond formation from the open to the closed state is described. Similarly in the last three terms all contributions which lead to an increase in concentration c_i due to association and dissociation processes are described. In Eq. 23 the dynamics of the closed pentameric ring state is separately described. In the derivation of Eq. 22 from Eq. 21 the symmetry of the matrices $k_\pm^{i,l} = k_\pm^{l,i}$ has been exploited. The above described set of ODEs obeys mass conservation ($\sum_i (c_i + \delta_{i,5}c_5^\star)i = \text{const}$). Thus, one of the concentrations could be eliminated as it is dependent on the other concentrations.

3. Comparison between rate equations and BD simulations

After having defined the macroscopic rate equation approach for the changes in fragment concentration in Eq. 22, we will now compare our BD simulation results to the macroscopic rate equation approach. As all macroscopic rates are fully specified by the microscopic parameters (Eq. 19 and Eq. 20), the comparison between the simulation and macroscopic

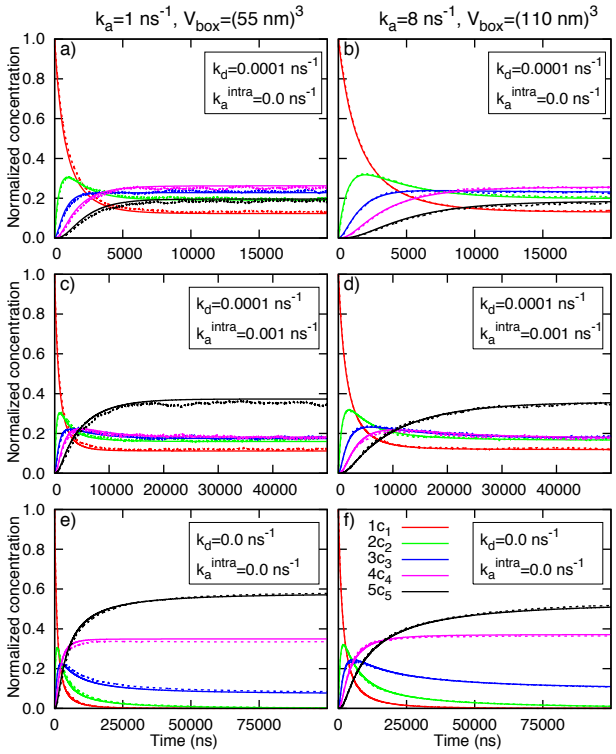

FIG. 9. Comparison of the rate equation approach Eq. 22 (solid lines) and the BD algorithm (dashed lines). The evolution of the normalized concentrations of the ring fragments $\tilde{c}_i = \frac{ic_i}{c_0}$ with $c_0 = N/V$ are shown for different parameters. All simulations were started with $N = 500$ individual proteins with a time resolution of $\Delta t = 0.01$ns and the simulation results have been averaged over 40 independent trajectories. The left column corresponds to reaction-limited assembly with $k_a = 1\text{ns}^{-1}$ and $V_{\text{box}} = (55\text{nm})^3$. The right column corresponds to diffusion-influenced assembly with $k_a = 8\text{ns}^{-1}$ and $V_{\text{box}} = (110\text{nm})^3$ in which the increase in k_a is balanced by the decrease in concentration. In a) and b) the result for a reversible reaction with a dissociation rate of $k_d = 0.0001\text{ns}^{-1}$ and without internal bond formation is ($k_a^{\text{intra}} = 0.\text{ns}^{-1}$) shown. In c) and d) the final ring is additionally stabilized by the formation of an internal bond with rate $k_a^{\text{intra}} = 0.001\text{ns}^{-1}$ (see Eq. 15). In e) and f) the evolution of the cluster size distribution is shown for irreversible binding ($k_d = 0\text{ns}^{-1}$).

theory does not involve any free parameter. For the BD simulations we randomly position $N = 500$ single proteins in a periodic box of size V_{box} and record the time-course of the fragment concentrations. All BD simulations were performed at a timestep resolution of $\Delta t = 0.01$ns and the resulting concentrations were averaged over 40 independent trajectories.

For the comparison with the rate equation approach we use an initial concentration of $c_0 = c_1(t = 0) = N/V$. Here V is the accessible simulation volume which is roughly estimated from the box volume by $V = V_{\text{box}} - (N-1)4\pi(2R)^3/3$.

In Fig. 9 the evolution of the normalized fragment concentrations $\tilde{c}_i = (c_i + \delta_{i,5}c_5^\star)i/c_0$ is shown. The normalized concentration of a fragment is defined as the concentration c_i weighted by the number of proteins contained in the fragment and normalized by the initial concentration. The normalized concentration predicted by the rate equation approach is shown with solid lines, while the averaged simulation results are represented by dashed lines. In the left column of Fig. 9 (Fig. 9 a,c and e) a microscopic reaction rate of $k_a = 1\text{ns}^{-1}$ and a box volume of $V_{\text{box}} = (55\text{nm})^3$ are chosen. As the diffusive off-rates range from $k_{D,b}^{1,1} \approx 8.2\text{ns}^{-1}$ to $k_{D,b}^{2,3} \approx 4.2\text{ns}^{-1}$, this assembly process can be considered as reaction-limited ($k_a < k_{D,b}$). In the case of a reaction-limited process, the macroscopic off- and on-rates given in Eq. 19 and Eq. 20 simplify to $\tilde{k}_+^{i,j} \approx k_D^{i,j}/k_{D,b}^{i,j}k_a = V_{i,j}^\star k_a$ and $\tilde{k}_-^{i,j} \approx k_d$. Thus, in this case the rates only depend on the microscopic reaction rates and of the encounter volume $V_{i,j}^\star$. In the right column of Fig. 9 (Fig. 9 b,d and f) a microscopic association rate of $k_a = 8\text{ns}^{-1}$ is chosen. This 8-fold increase in the microscopic association rate is compensated by an 8-fold decrease in concentration. In this case the reaction is strongly affected by diffusion ($k_a \geq k_{D,b}$) and the macroscopic rates crucially depend on the different diffusive on- and off-rates $k_D^{i,j}$ and $k_{D,b}^{i,j}$, which vary with the diffusive properties of the different fragments as can be seen in Tab. II and a clearly different assembly dynamic is expected. We will refer to this case as diffusion-influenced assembly.

In Fig. 9a and Fig. 9b the normalized fragment concentrations for the assembly with reversible bonds ($k_d = 0.0001\text{ns}^{-1}$) but without an additional stabilization of the full ring structure ($k_a^{\text{intra}} = 0$) is shown. Comparing the predictions from the rate equation approach (Eq. 22) (solid lines) with the averaged simulation results (dashed lines) we observe excellent agreement between our simulation results and the results from the macroscopic rate equation approach in the reaction-limited regime as well as in the strongly diffusion-influenced regime. The small deviations between the simulation results and the rate equation approach in Fig. 9a can be explained by our rough estimate for the excluded volume. This agreement between the two approaches, especially for the diffusion influenced regime is remarkable and demonstrates that, by evaluating the relevant diffusive properties of the fragments, we are indeed able to relate our microscopic reaction parameters to macroscopic reaction rates that

correctly reproduce the dynamics of the system. Comparing the equilibrium distribution of the cluster fragments in Fig. 9a and Fig. 9b we see that indeed the 8-fold decrease in concentration is balanced by the 8-fold increase in concentration, as it was expected due to our previous reasoning. However, comparing the kinetics of assembly we see a clear difference between Fig. 9a and Fig. 9b. In general, the approach towards equilibrium is slower in Fig. 9b than in Fig. 9a. This shows that we are indeed in a different assembly regime and the change in concentration is not compensated by the change in k_a in the kinetics of the assembly process. At lower concentration (Fig. 9b) clusters need a longer time to find each other diffusively which is reflected in the slower approach towards equilibrium.

In Fig. 9c and Fig. 9d the normalized fragment concentrations with an additional stabilization of the final ring structure $k_a^{\text{intra}} = 10k_d = 0.001\text{ns}^{-1}$ is shown. As discussed previously, the internal bond formation can be understood as an intrinsic process which stabilizes the full ring (Eq. 23). The value chosen for the internal association rate corresponds to a free energy of $E \approx -2.3k_BT$ associated with the bond formation according to Eq. 15. In Fig. 9c and Fig. 9d, the normalized fragment concentration of the full ring (black line) is shown irrespective of the number of bonds in the ring. Comparing the simulation results and the rate equation approach we again observe very good agreement between them. Similarly to the case without internal bond formation (Fig. 9a and Fig. 9b), the assembly dynamics at lower concentration (Fig. 9d) is slower than at higher concentration (Fig. 9c), while the equilibrium steady state remains the same in both cases. In contrast to the reversible bond formation without additional stabilization of the ring (Fig. 9c and Fig. 9e) the normalized concentration of the full ring is significantly increased by the internal bond formation. Due to mass conservation the increase in the concentration of the full ring structure is balanced by a decrease in the concentration of smaller fragments showing how an additional internal state can alter the equilibrium cluster size distribution.

Finally, we investigate the assembly dynamics for irreversible bond formation ($k_d = 0\text{ns}^{-1}$) for two different microscopic reaction rates k_a corresponding to the regime of reaction-limited reactions (Fig. 9e) and diffusion-influenced reactions (Fig. 9f). Again the simulation results and the rate equation approach agree remarkably well with each other. By comparing Fig. 9e and Fig. 9f we again verify that the approach towards the steady state is much slower in the case of lower concentration shown in Fig. 9f. However, in contrast to the previously discussed reversible bond formation, the steady state is different in both cases

with different fraction of ring fragments containing 3,4 and 5 proteins. This reflects a fundamental difference between the steady state observed for reversible bond formation and the steady state observed for irreversible bond formation. In the case of reversible bond formation the steady state is an equilibrium state in which dissociation and association events balance each other. This state only depends on the microscopic reaction rates k_a and k_D and the size of the reactive volume $V^\star$ (Eq. 13). In contrast the steady state for irreversible bond formation is a trapped steady state without any underlying dynamics. In this case of irreversible bond formation the ring fragments cannot disassemble and fragments of size $i \geq 5/2$ cannot further assemble if all smaller fragments have been used up. Thus, in the case of trapping the final state depends on the kinetics of the assembly. The difference in the two steady states observed in Fig. 9e and Fig. 9f also shows that the assembly dynamics in Fig. 9f is not only slowed down compared to Fig. 9e, but that the different diffusive properties of the cluster fragments lead to a change in the ratio of the concentration of intermediates during the assembly process. In general, larger fragments are diffusing slower than smaller fragments, and hence the rate for a reaction between two larger fragments is more strongly affected by diffusion than the reaction rate for two smaller fragments. In Fig. 9f this results in a lower concentration of pentameric rings, as the reaction probability of two small fragments is less affected by diffusion than the reaction probability of a smaller and a larger fragment. This leads to a stronger depletion of small fragments and hence a higher concentration of trapped ring fragments with 3 or 4 proteins.

IV. CONCLUSION

Biological structures like the actin cytoskeleton [13–15] or the nuclear pore complex [7–9] are highly dynamic with their constituents being continuously exchanged. To understand the biological functionality of these fascinating systems, a detailed understanding of the assembly dynamics is crucial. Moreover, advances in the fabrication of colloidal particles with directed interactions ("patchy particles") allow to design a plethora of differently shaped building blocks with tunable interactions that can self-assemble into new materials. [18–23] To increase the yield of the desired structures encoded in the local particle interactions, kinetic trapping in unfavorable configurations during the assembly process has to be prevented. Recently it has been shown that particle interactions during the assembly process

can be actively controlled. [24, 25] Thus, by a state- or time-dependent switching of reactivity the assembly process can be actively steered to reduce kinetic trapping. However, to fully exploit the possibilities of controlling the assembly process, a detailed understanding of its full dynamics with the formation of assembly intermediates is necessary.

Here we presented a novel simulation approach which is ideally suited to investigate the dynamics of large protein assemblies with well-defined architectural properties. Proteins are represented by (multiple) non-overlapping, hard spheres equipped with reactive patches. In contrast to most previous studies on protein assembly [25, 56–63, 66, 67], which rely on force fields to describe protein interactions, we combine overdamped Brownian motion with the concept of reversible, stochastic reactivity for patchy particles. Each cluster is treated as rigid object with its diffusive properties being evaluated on-the-fly. If the reactive patches of two clusters form an encounter by force-free diffusive motion, a bond between the clusters is established with a predefined rate. Local rules are used to describe the resulting rearrangements, which are assumed to be very fast on the time scale of the BD simulations. For potential-based simulations, these rearrangements would proceed due to the corresponding forces, which do not exist in our approach. Similar to the association process, the dissociation process also occurs with a predefined rate. Here we have derived the rules for the placement of the two partners which are required to satisfy detailed balance.

Together, these rules render our approach very efficient because complexes formed during the assembly are diffusing as rigid objects (thus reducing the number of degrees of freedom to be propagated to six) and because interactions are treated locally (as opposed to evaluating potentials). Nevertheless, the patchy particle approach includes detailed information on the architecture of protein assemblies, thus allowing us to study the spatial-temporal dynamics of specific biological systems of interest. Moreover, we have been able to show how the microscopic reaction parameters used in our approach correspond to the macroscopic reaction rates commonly used to describe the dynamics of the concentration of assembly intermediates. This allows a direct comparison between macroscopic, experimentally measurable concentrations and simulation results. To the best of our knowledge, this is the first time that a BD algorithm combining stochastic reactivity of anisotropic patches with reversible dynamics that fulfills detailed balance is presented. Testing our algorithm against mean field prediction for the case of bimolecular reactions revealed the importance of satisfying detailed balance.

As an example for a multi-component cluster, we investigated the assembly of a pentameric ring. Here we compared our simulation results to a rate equation approach for the different fragment concentrations. By extracting the diffusive on- and off-rates from our simulations we find excellent agreement between the rate equation approach and our simulation results even for the case of strongly diffusion-influenced assembly without any free parameter. We showed that the assembly dynamics can be significantly changed by the change in the diffusive properties of the assembly intermediates. In the case of irreversible bond formation the system becomes trapped with incompatible ring fragments. In this case not only the assembly kinetics but also the finally reached steady state depends on the different diffusive properties of the assembly intermediates. For complex assembly geometries trapping is a common motif. Thus, in this case not only correctly predicted equilibrium structure distribution of the assembly intermediates is relevant but also the correctly predicted kinetics of the assembly process as the system might become trapped before reaching the expected equilibrium steady state. By demonstrating how the macroscopic reaction rates can be calculated from our simulation, we have developed a framework in which a qualitative prediction of the changes in the macroscopic reaction rates, based on the changes of the diffusive properties of the assembly intermediates, is possible.

Because our approach aims to describe the assembly of large protein structures, the details of individual bond formations are not resolved within this framework. In general, the use of local rules requires well-defined target geometries and the instantaneous local rearrangement accompanying stochastic bond formation follows from the assumption that the time scales of assembly and local rearrangements are well separated. Given the coarse-grained nature of our approach, the instantaneous rearrangement during binding is a valid approximation if the encounter volume specifies a narrow region around the desired configuration. In the case of large encounter volumes the assumption of fast and small local rearrangements can break down and the use of local rules needs to be considered with care. In particular in the case of higher protein densities or assembly close to a membrane this can lead to a situation in which physically reasonable rearrangements are suppressed by our steric rules. In classical MD or BD simulations with potentials, these rearrangements would be realized due to ensuing mechanical forces. Typical biological examples for situations which are out of the scope of our current approach are the bending of a membrane by BAR-proteins [81, 82], the emergence of polymorphic virus structures [83–85] or the assembly of actin

networks from preexisting large fibers [86]. In principle, such a situation could be resolved by using hybrid schemes that interface our approach with potential-based simulations for local rearrangements. For the time being, however, we focus on the assembly of protein complexes with well-defined architectures, like native viruses[87], centrioles [6, 88–90] or actin filaments in networks growing by incorporation of actin monomers from solution [14, 86, 91].

In the future, our approach can be used to study the assembly of such complex protein clusters. After we have successfully verified our approach by comparing averaged simulation data with macroscopic mean field results, we now can investigate the stochastic variance inherent to these self-assembly processes. Our approach is ideally suited to study the effect of time- or state-dependent changes in reactivity, as has been recently shown in a qualitative study on the effect on hierarchical assembly in virus capsids. [26] Moreover, this approach might also help to design artificial systems that do not get kinetically trapped in undesired structures. It can also be coupled with hydrodynamic schemes, in particular with reactive multi-particle collision dynamics [92].

ACKNOWLEDGMENTS

HCRK acknowledges financial support by the Cusanuswerk. USS is a member of the Heidelberg cluster of excellence CellNetworks. We thank Nils Becker and Joris Paijmans for helpful discussions.

[1] R. R. Gabdoulline and R. C. Wade, Biophysical Journal **72**, 1917 (1997).

[2] W. Roos, R. Bruinsma, and G. Wuite, Nature Physics **6**, 733 (2010).

[3] A. Zlotnick and S. Mukhopadhyay, Trends in Microbiology **19**, 14 (2011).

[4] D. A. Compton, Annual Review of Biochemistry **69**, 95 (2000).

[5] E. Karsenti, F. Nédélec, and T. Surrey, Nature Cell Biology **8**, 1204 (2006).

[6] P. Gönczy, Nature Reviews Molecular Cell Biology **13**, 425 (2012).

[7] F. Alber, S. Dokudovskaya, L. M. Veenhoff, W. Zhang, J. Kipper, D. Devos, A. Suprapto, O. Karni-Schmidt, R. Williams, B. T. Chait, *et al.*, Nature **450**, 683 (2007).

[8] M. A. D'Angelo and M. W. Hetzer, Trends in Cell Biology **18**, 456 (2008).

[9] E. J. Tran and S. R. Wente, Cell **125**, 1041 (2006).

[10] B. Geiger and A. Bershadsky, Current Opinion in Cell Biology **13**, 584 (2001).

[11] A. D. Bershadsky, C. Ballestrem, L. Carramusa, Y. Zilberman, B. Gilquin, S. Khochbin, A. Y. Alexandrova, A. B. Verkhovsky, T. Shemesh, and M. M. Kozlov, European Journal of Cell Biology **85**, 165 (2006).

[12] H. Wolfenson, Y. I. Henis, B. Geiger, and A. D. Bershadsky, Cell Motility and the Cytoskeleton **66**, 1017 (2009).

[13] C. C. Beltzner and T. D. Pollard, Journal of Biological Chemistry **283**, 7135 (2007).

[14] K. Guo, J. Shillcock, and R. Lipowsky, The Journal of Chemical Physics **131**, 015102 (2009).

[15] T. D. Pollard, Annual Review of Biophysics and Biomolecular Structure **36**, 451 (2007).

[16] K. Guo, J. Shillcock, and R. Lipowsky, The Journal of Chemical Physics **133**, 155105 (2010).

[17] G. Schreiber, G. Haran, and H.-X. Zhou, Chemical Reviews **109**, 839 (2009).

[18] C. A. Mirkin, R. L. Letsinger, R. C. Mucic, and J. J. Storhoff, Nature **382**, 607 (1996).

[19] L. Di Michele and E. Eiser, Physical Chemistry Chemical Physics **15**, 3115 (2013).

[20] Y. Wang, Y. Wang, D. R. Breed, V. N. Manoharan, L. Feng, A. D. Hollingsworth, M. Weck, and D. J. Pine, Nature **491**, 51 (2012).

[21] C. Knorowski and A. Travesset, Current Opinion in Solid State and Materials Science **15**, 262 (2011).

[22] S. Sacanna, W. Irvine, P. M. Chaikin, and D. J. Pine, Nature **464**, 575 (2010).

[23] S. Sacanna, M. Korpics, K. Rodriguez, L. Colón-Meléndez, S.-H. Kim, D. J. Pine, and G.-R. Yi, Nature Communications **4**, 1688 (2013).

[24] M. E. Leunissen, R. Dreyfus, F. C. Cheong, D. G. Grier, R. Sha, N. C. Seeman, and P. M. Chaikin, Nature Materials **8**, 590 (2009).

[25] L. Di Michele, F. Varrato, J. Kotar, S. H. Nathan, G. Foffi, and E. Eiser, Nature Communications **4**, 2007 (2013).

[26] J. E. Baschek, H. C. Klein, and U. S. Schwarz, BMC Biophysics **5**, 22 (2012).

[27] M. v. Smoluchowski, Zeitschrift für physikalische Chemie **92**, 9 (1917).

[28] F. C. Collins and G. E. Kimball, Journal of Colloid Science **4**, 425 (1949).

[29] K. Šolc and W. Stockmayer, International Journal of Chemical Kinetics **5**, 733 (1973).

[30] D. Shoup, G. Lipari, and A. Szabo, Biophysical Journal **36**, 697 (1981).

[31] O. Berg, Biophysical Journal **47**, 1 (1985).

[32] A. Shushin, The Journal of Chemical Physics **110**, 12044 (1999).

[33] M. Schlosshauer and D. Baker, The Journal of Physical Chemistry B **106**, 12079 (2002).

[34] M. Schlosshauer and D. Baker, Protein Science **13**, 1660 (2004).

[35] N. Agmon, The Journal of Chemical Physics **81**, 2811 (1984).

[36] N. Agmon and A. Szabo, The Journal of Chemical Physics **92**, 5270 (1990).

[37] S. H. Northrup, S. A. Allison, and J. A. McCammon, The Journal of Chemical Physics **80**, 1517 (1984).

[38] S. H. Northrup and H. P. Erickson, Proceedings of the National Academy of Sciences **89**, 3338 (1992).

[39] H. X. Zhou, Journal of Physical Chemistry **94**, 8794 (1990).

[40] H.-X. Zhou, Biophysical Journal **64**, 1711 (1993).

[41] R. R. Gabdoulline and R. C. Wade, Journal of Molecular Biology **306**, 1139 (2001).

[42] G. Zou and R. D. Skeel, Biophysical Journal **85**, 2147 (2003).

[43] R. Alsallaq and H.-X. Zhou, Structure **15**, 215 (2007).

[44] R. Alsallaq and H.-X. Zhou, Biophysical Journal **92**, 1486 (2007).

[45] S. Qin, X. Pang, and H.-X. Zhou, Structure **19**, 1744 (2011).

[46] M. Klann and H. Koeppl, International Journal of Molecular Sciences **13**, 7798 (2012).

[47] S. S. Andrews and D. Bray, Physical Biology **1**, 137 (2004).

[48] S. S. Andrews, Physical Biology **2**, 111 (2005).

[49] J. S. van Zon and P. R. Ten Wolde, The Journal of Chemical Physics **123**, 234910 (2005).

[50] M. J. Morelli and P. R. Ten Wolde, The Journal of Chemical Physics **129**, 054112 (2008).

[51] K. Takahashi, S. Tănase-Nicola, and P. R. ten Wolde, Proceedings of the National Academy of Sciences **107**, 2473 (2010).

[52] D. T. Gillespie, The Journal of Physical Chemistry **81**, 2340 (1977).

[53] J. Hattne, D. Fange, and J. Elf, Bioinformatics **21**, 2923 (2005).

[54] D. Fange, O. G. Berg, P. Sjöberg, and J. Elf, Proceedings of the National Academy of Sciences **107**, 19820 (2010).

[55] D. Fange, A. Mahmutovic, and J. Elf, Bioinformatics **28**, 3155 (2012).

[56] D. Rapaport, Physical Review Letters **101**, 186101 (2008).

[57] M. F. Hagan and D. Chandler, Biophysical Journal **91**, 42 (2006).

[58] H. D. Nguyen, V. S. Reddy, and C. L. Brooks III, Nano Letters **7**, 338 (2007).

[59] D. Rapaport, Physical Review E **86**, 051917 (2012).

[60] I. G. Johnston, A. A. Louis, and J. P. Doye, Journal of Physics: Condensed Matter **22**, 104101 (2010).

[61] C. Horejs, M. K. Mitra, D. Pum, U. B. Sleytr, and M. Muthukumar, The Journal of Chemical Physics **134**, 125103 (2011).

[62] A. W. Wilber, J. P. Doye, A. A. Louis, E. G. Noya, M. A. Miller, and P. Wong, The Journal of Chemical Physics **127**, 085106 (2007).

[63] A. W. Wilber, J. P. Doye, and A. A. Louis, The Journal of Chemical Physics **131**, 175101 (2009).

[64] J. Largo, F. W. Starr, and F. Sciortino, Langmuir **23**, 5896 (2007).

[65] P. F. Damasceno, M. Engel, and S. C. Glotzer, Science **337**, 453 (2012).

[66] X. Liu, J. C. Crocker, and T. Sinno, The Journal of Chemical Physics **138**, 244111 (2013).

[67] F. Sciortino, C. De Michele, and J. F. Douglas, Journal of Physics: Condensed Matter **20**, 155101 (2008).

[68] J. D. Halverson and A. V. Tkachenko, Physical Review E **87**, 062310 (2013).

[69] M. Eigen, *Diffusion control in biochemical reactions. In Quantum Statistcal Mechanics in the Natural Sciences*, edited by S. L. Mintz and S. M. Widmayer, Studies in the Natural Sciences, Vol. 4 (Plenum Press, New York and London, 1974) pp. 37–61.

[70] D. Shoup and A. Szabo, Biophysical Journal **40**, 33 (1982).

[71] C. Korn and U. Schwarz, The Journal of Chemical Physics **126**, 095103 (2007).

[72] J. Schluttig, D. Alamanova, V. Helms, and U. S. Schwarz, The Journal of Chemical Physics **129**, 155106 (2008).

[73] J. Schluttig, C. B. Korn, and U. S. Schwarz, Physical Review E **81**, 030902 (2010).

[74] J. García de la Torre, M. L. Huertas, and B. Carrasco, Biophysical Journal **78**, 719 (2000).

[75] B. Berger, P. W. Shor, L. Tucker-Kellogg, and J. King, Proceedings of the National Academy of Sciences **91**, 7732 (1994).

[76] T. L. Hill, *An Introduction to Statistical Thermodynamics* (Dover Publications, New York, 1986) (Unabridged, corr. republ. of the 2. print., Reading, Mass., 1962).

[77] M. Pogson, R. Smallwood, E. Qwarnstrom, and M. Holcombe, Biosystems **85**, 37 (2006).

[78] M. T. Klann, A. Lapin, and M. Reuss, BMC Systems Biology **5**, 71 (2011).

[79] J. Paijmans, *The Fundamental Lower Bound of the Noise in Transcriptional Regulation* (Master thesis, University of Amsterdam, Amsterdam, 2012).

[80] N. Kern and D. Frenkel, The Journal of Chemical Physics **118**, 9882 (2003).

[81] A. Arkhipov, Y. Yin, and K. Schulten, Biophysical Journal **95**, 2806 (2008).

[82] A. Frost, V. M. Unger, and P. D. Camilli, Cell **137**, 191 (2009).

[83] H. D. Nguyen and C. L. Brooks III, Nano Letters **8**, 4574 (2008).

[84] O. M. Elrad and M. F. Hagan, Nano Letters **8**, 3850 (2008).

[85] H. D. Nguyen, V. S. Reddy, and C. L. Brooks III, Journal of the American Chemical Society **131**, 2606 (2009).

[86] L. Blanchoin, R. Boujemaa-Paterski, C. Sykes, and J. Plastino, Physiological Reviews **94**, 235 (2014).

[87] D. L. D. Caspar and A. Klug, in *Cold Spring Harbor Symposia on Quantitative Biology*, Vol. 27 (Cold Spring Harbor Laboratory Press, 1962) pp. 49–50.

[88] D. Kitagawa, I. Vakonakis, N. Olieric, M. Hilbert, D. Keller, V. Olieric, M. Bortfeld, M. C. Erat, I. Flückiger, P. Gönczy, and M. O. Steinmetz, Cell **144**, 364 (2011).

[89] M. van Breugel, M. Hirono, A. Andreeva, H.-a. Yanagisawa, S. Yamaguchi, Y. Nakazawa, N. Morgner, M. Petrovich, I.-O. Ebong, C. V. Robinson, C. M. Johnson, D. Veprintsev, and B. Zuber, Science **331**, 1196 (2011).

[90] P. Guichard, V. Hachet, N. Majubu, A. Neves, D. Demurtas, N. Olieric, I. Fluckiger, A. Yamada, K. Kihara, Y. Nishida, S. Moriya, M. O. Steinmetz, Y. Hongoh, and P. Gönczy, Current

Biology **23**, 1620 (2013).

[91] C. Erlenkämper and K. Kruse, The Journal of Chemical Physics **139**, 164907 (2013).

[92] R. Kapral, The Journal of Chemical Physics **138**, 020901 (2013).